Self-seeded growth of very large open-structured zeolite nanosheet assemblies with extraordinary micropore accessibility

Zishu Cao [a], Landysh Iskhakova [a], Xinhui Sun [a], Ninad D. Anjikar [b], Shaowei Yang [b], Junhang Dong [a],*

[a] *Department of Chemical and Environmental Engineering, University of Cincinnati, Cincinnati, OH, 45221, USA*
[b] *Department of Chemical and Biomedical Engineering, Cleveland State University, Cleveland, OH, 44115, USA*

A R T I C L E   I N F O

A B S T R A C T

Zeolite nanosheets (ZNs) offer improved micropore accessibilities and transport properties for enhanced molecular catalysis and separations. However, practical application of the ZN materials is hampered by the lack of efficient synthesis methods. Here, a ZN self-seeded method is demonstrated for single-step reproduction of flower-like assemblies of very large MFI ZN plates. The ZN plates are ~60 nm-thick stacks of 4-nm-thick single-crystal sheets. The ZN flower growth involves terrace nucleation on the seed surfaces and subsequent ZN epitaxial growth in [010] orientation directed by a diquaternary agent. The open architecture of the assemblies prevented collapse and agglomeration of ZNs during thermal activation that effectively preserved the interconnected intra-sheet and inter-sheet micropore system. Thus, the ZN assemblies exhibited markedly enhanced molecular adsorption capacity and transport diffusivity for the probing xylene molecules as compared to the conventional crystals. The ZN assembly and its harvestable very large-sized ZNs have the potential for developing high-performance ZN adsorbents, catalysts, and molecular-sieve membranes.

1. Introduction

Zeolites are crystalline aluminosilicates containing ordered pores of molecular dimensions well-suited for molecular catalysis and separations in petrochemical, biochemical reaction, and energy production processes. In recent years, there have been successful syntheses of two-dimensional (2D) zeolite nanosheets (ZNs) with thicknesses of one or two unit-cells [1–4]. These 2D ZNs maximize the accessibility of active surface sites and micropores for adsorbing molecules and catalyzing reactions. Meanwhile, the ultrathin ZNs minimize the diffusion length that overcomes molecular transport limitations in catalysis and separation processes [1,5]. The 2D ZNs and their hierarchical assemblies thus offer significantly enhanced performances in heterogeneous catalysis and molecular separations [3,6–11]. The 2D ZNs with large lateral-to-thickness aspect ratios can also laminate ultrathin membranes of desired orientations to reduce the transmembrane diffusion resistance and nonselective intercrystalline entrances leading to simultaneous improvements in permeability and selectivity [4,12–16].

Despite the tremendous potentials demonstrated on small-sized samples, the development of practical ZN adsorbents, catalysts, and membranes has been hampered by the lack of methods for efficient synthesis of redispersible activated ZNs with well-preserved micropore accessibility and surface properties. In the literature, MWW and MFI ZNs with thickness of one- or two-unit cells were obtained by exfoliation from layered zeolite precursors (LZP) synthesized using diquaternary or triquaternrny ammonium structure directing agents (SDA) [12,17,18]. The exfoliated single crystalline ZNs are typically 100–400 nm in lateral lengths. These small-size ZNs tend to aggregate and deform that cause difficulties in reassembling useful macrostructures. Recently, a nanoparticle-seeded secondary growth method was developed to directly produce isolated single crystalline MFI ZNs using diquaternary bis-1,5(tripropyl ammonium) pentamethylene diiodide (dC$_5$) as the SDA [4]. However, the as-synthesized ZN crystal contains an isotropic core grown from the spherical seed, which must be eliminated by tedious processes to achieve flat ZNs [12,15]. The LZP exfoliation and seeded secondary growth methods are both prohibitively complex with extremely low yields. The difficult redispersion of activated ZNs also limits the fabrication of ZN-laminated membranes on economical polymer substrates [14,16].

Herein, we report a self-seeded single-step synthesis method for

* Corresponding author.
E-mail address: dongj@ucmail.uc.edu (J. Dong).

efficient reproduction of flower-like ZN-assemblies comprising very large single-crystal nanosheets of two unit-cells in thickness. Microscopic investigations were carried out to understand the ZN-seeded crystal growth mechanisms and unveil the microstructure and pore system of the ZN and ZN assemblies. The ZN materials were demonstrated with markedly enhanced molecular adsorption and transport properties using xylenes as probing molecules.

2. Experimental section

2.1. Self-seeded synthesis of ZN-assemblies

Synthesis of first-generation ZN-assemblies. The pure-silica MFI (silicalite) ZNs used as seeds for growing the first-generation ZN-assemblies were synthesized by the method reported by Jeon et al. [4]. These ZN seeds were obtained by two separate steps of hydrothermal reactions. The first step was to generate silicalite nanoparticles (ZNP, ~30 nm dia.) using tetrapropylammonium hydroxide (TPAOH) as SDA; and the second step was to grow single crystalline silicalite ZNs using dC_5 as SDA. The detailed synthesis procedure was described in our previous work [15] and is schematically depicted in Fig. S1 together with microscopic images revealing the mechanism of ZNP-seeded ZN growth. The thus-synthesized zeolite ZN crystals were rhombus-shaped with each containing a seed-evolved high core encircled by a uniform nanosheet of 4-nm in thickness (Fig. S1b) [15].

These as-synthesized rhombus zeolite ZN crystals were soaked in a KOH cleaning solution containing 0.1 M KOH and 1 M KCl (pH = 12.98) and gently stirred for a week. The KOH solution was replaced twice during the 1-week period and then thoroughly washed by DI water. This aggressive and thorough cleaning process was necessary firstly to remove the amorphous silica and organic residues adsorbed on ZN surfaces, which could shield the active nucleation sites; and secondly to cleavage surface Si–O–Si that could create $[\equiv Si - O^{(-)}]$ sites to induce nucleation in different orientations [19,20]. The rhombus sheets were then broken up by sonicated ball-milling. The fractured flat ZN fragments were separated from the large core debris by centrifugation followed by further ball-milling to generate smaller ZN flakes for greater seed population. These seed ZNs was dispersed in a synthesis solution at a precursor-to-seed ratio of >500 on the basis of silicon mass. The synthesis solution had a dilute molar composition of 80 TEOS: 3.75 dC_5: 20 KOH: 12000 H_2O to avoid undesirable nucleation and inhibit random growth [21,22]. The ZN-seeded precursor was placed in an autoclave for autogenous reaction at 140 °C. After certain reaction durations, the products were separated by centrifugation and then thoroughly cleaned by the KOH solution before drying and characterizations.

Self-seeded reproduction of ZN-assemblies. After obtaining the above first-generation ZN assemblies, a facile single-step reaction process was demonstrated for efficiently reproducing next generations of ZN assemblies. This single-step synthesis was accomplished by secondary growth of ZN seeds in the same dilute precursor solution. The major difference was that the ZN seeds for next generations of ZN-assemblies were simply the ball-milled ZN fragments of the prior generation ZN assemblies but not the tediously synthesized single-crystal ZNs. These ZN seeds from the assemblies of last generations were also extensively cleaned by the KOH solutions to ensure the activity of the surface nucleation sites. In this work, after the first generation, such self-seeded reproduction of the ZN-assemblies was demonstrated by two consecutive generations with each used ZN seeds from the prior generation.

2.2. Material characterizations

The morphological and microstructural characteristics of the flower-like MFI ZN assemblies and crystals of different growth stages were investigated by scanning electron microscopy (SEM) and energy dispersive X-ray spectroscopy (EDS) using a FEI Scios DualBeam microscope equipped with Ametek Octane Super EDAX. The thicknesses of

the ZN plates constituting the ZN-assemblies and the isolated single-crystalline ZN sheets were examined by a Veeco Dimension 3100 atomic force microscope (AFM) using height imaging/profiling under tapping mode. The crystalline phase and orientation of the ZNs were identified by X-ray diffraction (XRD) using a PANalytical X'Pert Pro diffractometer with Cu Kα radiation (λ = 1.5406 Å) and confirmed by transmission electron microscopy (TEM) and electron diffraction (ED) observations using a JEOL 2010F field emission electron microscope. The XRD peak identification and crystal phase determination were based upon the standard spectrum of silicalite powders [23]. The high-resolution TEM observations were also used to unveil the mechanisms of ZN-assembly formation and growth in the very early stages.

The porosity and surface area of the ZN-assemblies were examined by the N_2 adsorption-desorption isotherms using an Miromeritics ASAP 2020 unit. The N_2 adsorption-desorption measurements were carried out for the ZN assemblies at 77 K before and after calcination at 873.15 K for 8 h for SDA removal. The dynamic adsorption behaviors of p-xylene and o-xylene vapors on the ZN-assemblies were investigated at 300 K by a Cahn 1000 Microbalance. The zeolite sample was degassed at about 573.15 K for overnight before each adsorption test. The gas phase xylene vapor pressure was around 0.67 kPa (or p/p° ~ 0.5). The xylene adsorption data were used to analyze the accessibility of the micropores and mesopores in the ZN-assemblies. A sample of conventional silicalite crystals was also examined by the BET and xylene adsorption measurements for comparisons. The conventional silicalite crystals were synthesized by our previously reported procedure using an Al-free clear solution of TEOS as silica source and TPAOH as SDA [24]. Both the ZN assembly and conventional crystal samples were thoroughly cleaned by the KOH solution before calcination activation. Before each adsorption measurements, the samples were dried at 393.15 K in a vacuum oven and further degassed at 523.15 K for 2.5 h during measurements. These deep cleaning and evacuation processes were used to completely remove the amorphous silica and organic residues from the ZN surfaces and intra- and inter-ZN layer nonzeolitic pores.

3. Results and discussion

3.1. ZN-seeded secondary growth

The seeds used for growing the first-generation ZNs and ZN assemblies were single crystalline silicalite ZN flakes of submicron lateral lengths and 4-nm thickness in its *b*-axis (Fig. 1A). The ball-milling of the ZN seeds not only increased the seed population for improving productivity but also created freshly fractured ZN edges containing highly energetic sites to induce secondary growth.

To investigate the secondary crystallization behavior of the ZN seeds, the solid products were retrieved after different reaction durations, which were microscopically analyzed. After reacting for 12 h, the seed ZNs, which had irregular shapes and sizes around ~0.1 μm² (Fig. 1A), grew into rhombus sheets with areas of ~0.50 μm² in average (Fig. 1B). The rhombus sheets had a uniform thickness of ~4 nm (Fig. S2A&B), that was the same as the ZN seed. This early-stage growth was largely epitaxial in *a-c* plane (same as the seed ZN) directed by the dC_5 SDA. The SDA inhibits growth in *b*-axis by the strong stresses from the dimensional mismatch between inter-quaternary space (C_5) of dC_5 and neighboring intersection-distance of the MFI framework [21]. The ZN seed seemingly formed a 10–20 nm tall central plateau in the premature rhombus sheet (Fig. S2A&B). Large amounts of nanoparticles were observed in the product after the 12-h reaction (Fig. 1B). These particles were largely amorphous as they could be readily dissolved in the KOH solution (Fig. S2C&D). Similar nanoparticles were seen in the literature during syntheses of MFI ZN with quaternary ammonium SDA and such particles were believed to be precursors for nucleation and crystal growth on seed surfaces [4,21]. The TEM image and inserted ED pattern in Fig. 1C show that the ZN sheet had a smooth surface with thickness along the [010] (*b*-axis) direction.
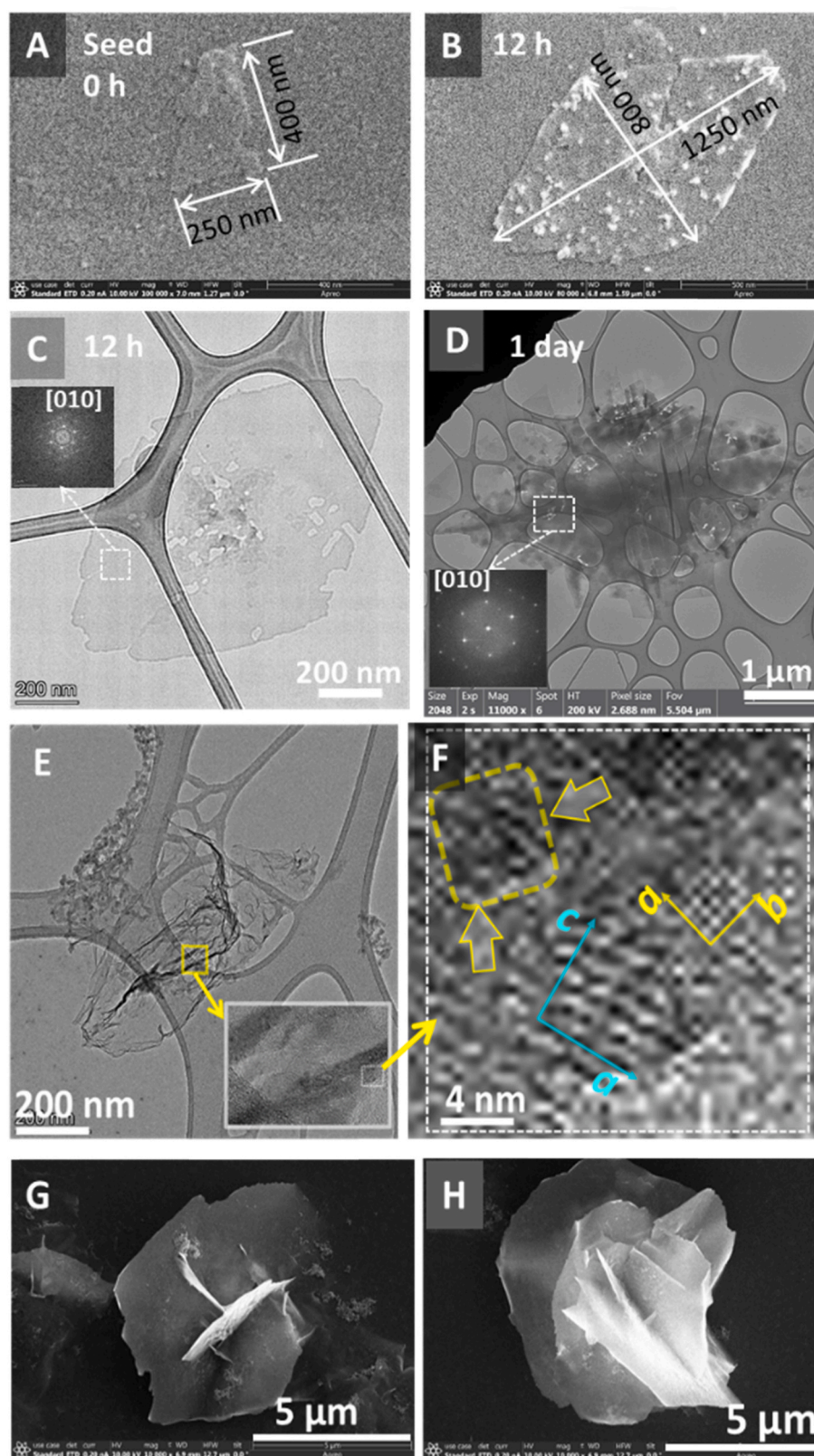
Fig. 1. Process of ZN seed growth into flower-like ZN-assembly: (A) SEM of a typical ZN fragment seed; (B) and (C) are SEM and TEM images of a typical rhombus sheet obtained in 0.5-day reaction; (D) TEM image of a rhombus sheet obtained by 1-day reaction; (E) TEM image of an extensively cleaned ZN from 1-day reaction; (F) high resolution (HR) TEM image of a local spot in the sample of (E); (G) and (H) are SEM images of typical crystals after growing for 2 and 3 days, respectively.

When the reaction duration was extended to 1 day, the rhombus sheets further grew to sizes of ~7.5 μm^2 with noticeable changes microstructure as shown by the TEM images in Fig. 1D. Unlike the smooth-surfaced sheet after 12-h reaction, the rhombus sheet from 1-day reaction exhibited microscopic features of densely populated discrete nanoparticles and emerging ZNs in orientation orthogonal to the base ZN surface (Fig. S3A&B). To examine the microscopic and crystalline structure of the rhombus sheet surface, the sample was treated by another 1-week of sonication in the KOH solution to eliminate amorphous particles and possible loosely attached nanocrystals. Fig. 1E is the TEM image of an intensively cleaned ZN fragment which appeared to be free of particulate in the ZN surface seen in Fig. 1D. However, the high-resolution TEM image in Fig. 1F unveiled nanodomains of distorted lattice in the ZN surface (pointed by arrows) and nuclei with *a-c* plane oriented normally to the seed surface (i.e., orthogonal growth from seed surface). For example, as indicated in Fig. 1F, the isolated domain of lattice in [010] direction likely reflected the *a-c* plane surface of the base ZN; and the nanodomain displaying [100] lattice structure showed a nucleus grown in rotated (orthogonal) orientation from the seed surface. Fig. 1G and H shows the further developed orthogonal ZN plates that are typical in samples produced by 2 and 3 days of reaction, respectively. The [100]-oriented nuclei apparently initiated the orthogonal growth of the ZNs. The steps of ZN self-seeded nucleation, orthogonal ZN evolution, and the subsequent ZN epitaxial growth into the very large flower-like ZN assembly are schematically illustrated in Fig. S4.

The premature structures in Fig. 1G and H and the amorphous nanoparticles were no longer observable after 4 days of reaction (Fig. 2). Further extension of the reaction duration to 6 days caused no appreciable changes in structure and size of the ZN assemblies. Thus, the structural characterizations and material property analyses were performed for samples obtained by 4 days of hydrothermal growth from the ZN seeds shown in Fig. 2A. The final NZ assemblies obtained in 4 days were of two distinct architectures in which the ZN plates (resembling flower petals) were organized in rose flower structure (Fig. 2B) and spiral leaf arrangement (Fig. 2C), respectively. The flower-like assemblies had overall diameters of >15 μm, which is unprecedented in such

an open structure. The ZN plate petals could be readily dissociated by sonicated ball-milling to harvest flat ZN plates of large areas. Fig. 4D shows unfractionated flat ZN plates with typical areas larger than 1.5 μm × 2.5 μm, which were obtained by sonication in water assisted by φ-4mm zirconia milling-beads.

3.2. Single-step ZN assembly reproduction

After obtaining the first-generation flower-like ZN assemblies, a single-step synthesis method was demonstrated for reproducing next generations of ZN flowers, as depicted in Fig. 3A. This facile cyclic reproduction was seeded by small-sized ZN fragments recovered from the dissociated ZN plates of the prior generation. The small ZN fragments shown in Fig. 3B from the first-generation (Fig. 2D) were used as seeds for growing the second-generation ZN flowers (Fig. 3C); and fragments shown in Fig. 3D from the second-generation were used as seeds for the third-generation ZN flowers (Fig. 3E). The ZN seeds in Fig. 3B and D were mostly <0.5 μm in side-lengths that could be further ball-milled to increase the seed population. The precursor solution of dilute dC$_5$ SDA and TEOS was the same as that used in synthesis of the first-generation ZN assemblies, and the hydrothermal secondary growth was conducted at 140 °C for 4 days in all cases.

3.3. Microstructure of the ZN plates in assemblies

The ZN plates separated from the flower-like assemblies were multilayered as unveiled by the TEM image and ED pattern (insert) of the plate edge shown in Fig. 4A. These multilayered ZN plates consisted of single crystal sheets as can be observed in the TEM images of Fig. 4B. The ED patterns in Fig. 4A and B indicate that the individual single crystal ZN sheet had thickness in *b*-axis direction. The ED pattern in Fig. 4A reflects overlapping ZN layers of [010] orientation (i.e., in *b*-axis direction); and ED pattern and lattice dimension in Fig. 4B confirm the [010] orientation of the single crystal sheet. The XRD spectra in Fig. 4C for the randomly packed ZN flowers and a glass-supported single layer ZN plates confirm the pure MFI zeolite phase and out-of-plane
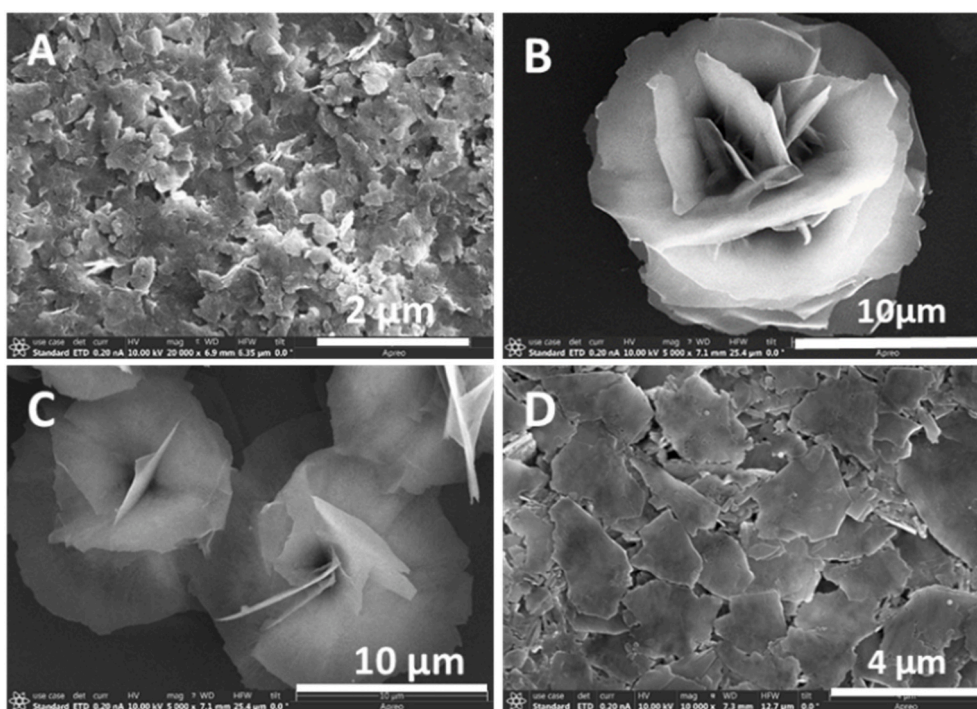

Fig. 2. The first-generation flower-like ZN assemblies: (A) seeds of ball-milled single crystalline ZNs prepared by reference method [4]; (B) a ZN assembly of rose-like architecture, (C) ZN assemblies of spiral leaf structure, and (D) unfractionated flat ZN plates disintegrated from the ZN flowers by ball-milling.
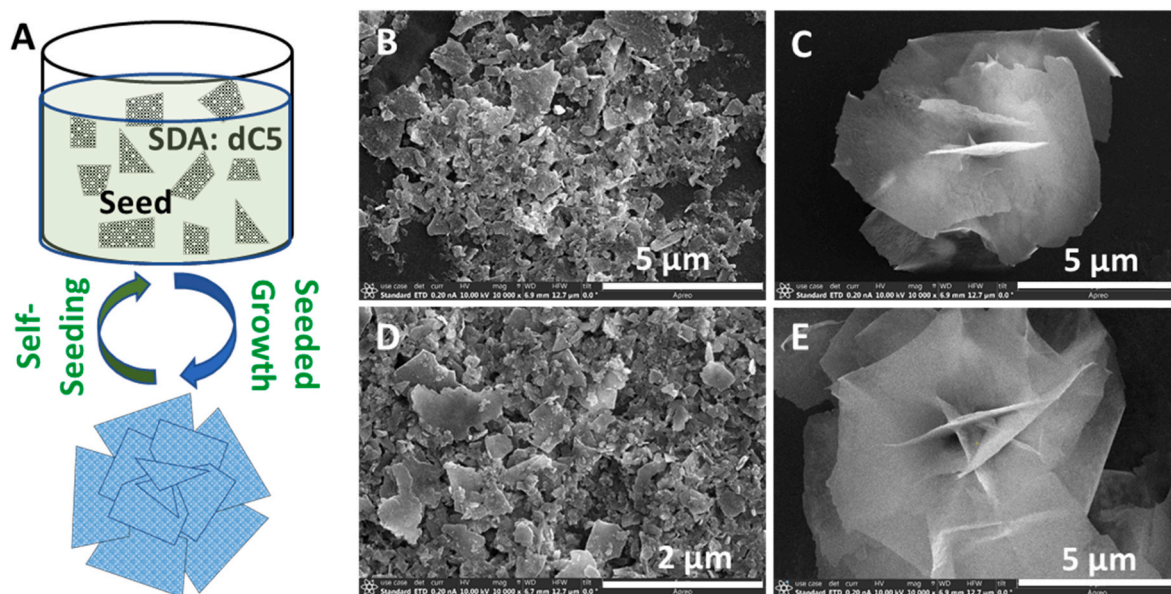
Fig. 3. Single-step growth of ZN assemblies by self-seeding with ground ZN plates: (A) schematic showing the self-seeded cyclic reproduction of ZN flowers; (B) small fragment seeds from the 1st generation flowers; (C) the 2nd generation ZN flower; (D) small fragment seeds from second-generation flowers, and (E) the 3rd generation ZN flowers.
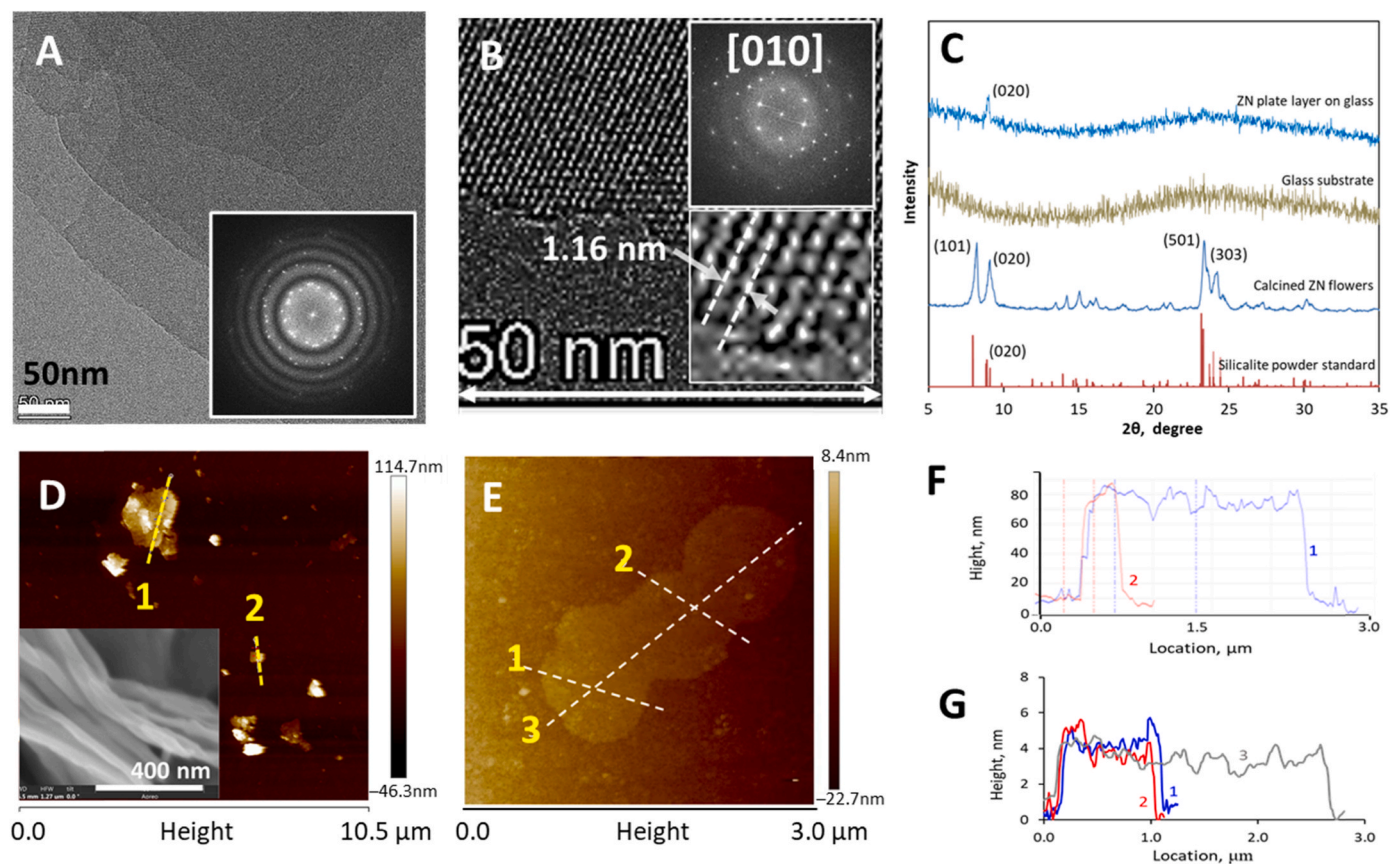

Fig. 4. Microstructure of ZN plates forming the flower-like assemblies: (A) TEM image and ED pattern of a multilayered plate edge; (B) TEM images and ED pattern of an exfoliated single-crystal sheet; (C) XRD spectra of the ZN flowers and a layer of flat ZN plates; (D) AFM height survey over the areas of multilayered ZN plates (insert: side-view SEM of a layer with multiple ZN plates); (E) AFM height survey over the area of a single crystal ZN sheet; and (F) and (G) are height-profiles of the multilayered ZN plates and the single crystal sheet along lines in (D) and (E), respectively.

orientation in *b*-axis for the flat ZN plates. The AFM height profiling results in Fig. 4D and F showed an average thickness of ~60 nm for the multilayered ZN plates. This thickness was in reasonable agreement with SEM observation on the cross-section of a ZN plate layer (insert in Fig. 4D). Exfoliation of the multilayered ZN plates did not happen during the sonicated treatments in the KOH solution. However, very limited exfoliation of the ZN-stacked plates occurred when the TPAOH was added into the KOH solution that generated some isolated single crystal

ZN sheets. These single-layer nanosheets (Fig. 4E) had typical dimensions of 1.0 μm × 2.5 μm with uniform thicknesses of around 4 nm (Fig. 4G) that gave aspect ratios of length/thickness (L/δ) ~ 600 and width/thickness (W/δ) ~ 250.

3.4. ZN-assembly pore system and xylene adsorption behavior

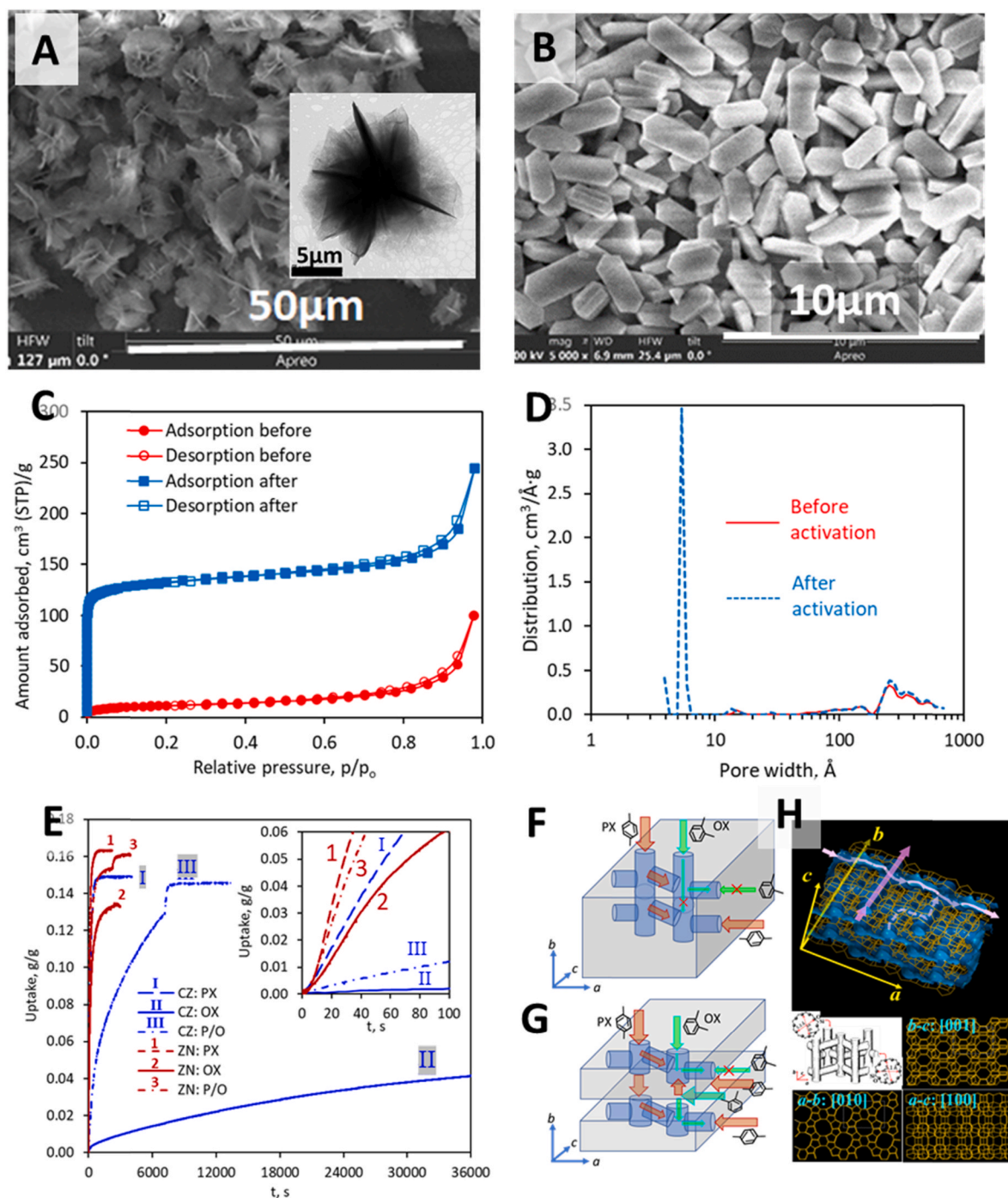The flower-like ZN assemblies were structurally stable during SDA

Fig. 5. (A) SEM picture of flower-like ZN assemblies after thermal activation and adsorption tests (insert TEM image showing flower-structure integrity); (B) SEM picture of conventional silicalite crystals; (C) N$_2$ adsorption-desorption curves for the ZN flowers before and after activation; (D) pore size distributions of the ZN flowers before and after activation; (E) dynamic adsorption curves for p-xylene, o-xylene, and equimolar p-xylene/o-xylene mixture vapors on the ZN assemblies and conventional silicalite crystals at 300 K and p/p^o ~ 0.05; (F) schematic showing accessibility of zeolitic pores to p-xylene and o-xylene molecules in conventional crystals; (G) schematic showing accessibility of intra- and intercrystalline micropore system to p-xylene and o-xylene molecules in the multilayered ZN plates; (H) topological structure of the 3D channel system in MFI zeolite crystals [23].

removal by calcination at 600 °C and multiple cycles of adsorption-desorption tests. The flower-like open structures prevented the assembled ZN plates from collapsing that consequently preserved the inter-ZN spaces for facilitated molecular transport. Fig. 5A presents the SEM and TEM images that corroborate the structural integrity of the activated ZN assemblies. The ZN assembly sample in Fig. 5A were examined for its pore structure and molecular adsorption and transport properties in comparison with the conventional micron-sized silicalite crystals shown in Fig. 5B.

Fig. 5C shows the N_2 adsorption-desorption isotherms at 77 K for the ZN assembly sample before and after thermal activation. The BET surface areas of the ZN assemblies were 42 and 492 m^2/g before and after SDA removal, respectively. The nonactivated ZN assemblies contained micropores with pore widths (d_p) of 1.09–1.85 nm and two groups of mesopores with d_p ranges of 4.7–17 nm and >19 nm, respectively (Fig. 5D). The microporosity may be attributed to the intracrystalline defects and spaces between misaligned single crystal sheets [2], i.e., inter-sheet spaces evolved from defects in the nucleus surface (Fig. S3D). As shown in Fig. 4G, the single crystalline sheet was microscopically uneven with thickness varying between 3 and 4 nm that could form inter-sheet spaces of 1–2 nm in width; and the mesoporosity was mainly inter-ZN plate spaces and some intracrystalline defects. The activated ZN assemblies exhibited a large volume of micropores with uniform d_p ~0.55 nm. This activated porosity corresponds to the MFI zeolitic channel sizes, i.e., the 0.53nn × 0.56 nm straight channels along *b*-axis and 0.51nm × 0.55 nm zigzag channels running in the *a-c* plane (Fig. 5H). The activated ZN assemblies also had nonzeolitic micropores and mesopores with size distributions virtually identical to those existed in the nonactivated sample. According to the t-plots (Fig. S5) from the 77 K N_2 adsorption isotherms in Fig. 5C, the micropore volume of the ZN assemblies was very small (<0.001 cm^3/g) before thermal activation and exhibited a large value of 0.187 cm^3/g after activation. This indicates that the inter-sheet micropores and inter-plate mesopores were well preserved after the thermal activation.

On the other hand, the microporosity with d$_p$ of 1.09–1.85 nm and mesoporosity with d$_p$ of >4.7 nm were not observed in the conventional crystals (Fig. S6) that further evidenced the unique inter-sheet and inter-plate pore system in the ZN assemblies. However, the conventional crystals contained more mesopores with d$_p$ of ~2.7 nm after 1-week treatment by the KOH solution than the ZN assemblies which exhibited an insignificant peak in Fig. S6B. Such mesopore defects are common in large-size MFI zeolite crystals after leaching by strongly alkaline solutions. The conventional silicalite crystals had a BET surface area of 376 m^2/g which is typical [25]. The difference in BET area between the multilayered-ZN assemblies and conventional crystals was consistent with literature findings on the silicalite LZP assemblies, which was also attributed to the preserved inter-lamellar microporosity in the LZP [1]. The BET surface area of the current ZN assemblies was slightly smaller than that of the LZP (520 m^2/g) [1] because the latter had smaller single sheet thickness (δ~2 nm) to form more inter-sheet boundaries.

To examine the accessibility of the zeolitic pores in the assemblies of multilayered ZN plates, dynamic adsorption was measured for p-xylene and o-xylene vapors at ~300 K under a relative vapor pressure (p/p^o) of ~0.5 (where saturation pressure $p^o = 1.3$ kPa). The xylene dynamic adsorption curves are presented in Fig. 5E. The zigzag channels in *a-c* plane are inaccessible to the larger o-xylene but can be entered by the smaller p-xylene while the straight channels are accessible to both xylenes [12,17,26,27]. Thus, xylenes are particularly suitable for probing the zeolitic pore accessibility in the ZN plates. Fig. 5F and G depict accessible paths for xylene to enter the zeolitic channels in conventional crystals and ZN plates, respectively. Fig. 5H shows the simulated topological structure of the interconnected MFI channel system [23]. The dynamic adsorption curves in Fig. 5E show that the ZN-assemblies had markedly greater adsorption amounts and faster uptake rates for the critically sized xylenes as compared to the conventional MFI crystals.

Table 1 summarizes the equilibrium loading of xylene molecules per

Table 1

Xylene equilibrium loading and apparent transport diffusivity in the ZN assemblies and conventional crystals at 303.15 K and relative vapor pressure of 0.5

Vapor	Ads. Loading (molc./u.c.)		D_T (10^{-16} m^2/s)	
	ZN-assembly	Conventional	ZN-assembly	Conventional
p-xylene	8.8	8.1	238–662	415–722
o-xylene	7.3	6.0	64.4–179	0.95–1.65
p-/o-xylene Mix	8.7	7.9	179–498[a]	16.6–28.9[a]

[a] Pseudo D_T for xylene mixture vapor.

unit cell (molc./u.c.) and the xylene apparent transport diffusivity (D_T) estimated by the uptake equation using the conventional characteristic radius (= $3V_p/A_p$) for particles of consideration [28,29]. The MFI zeolites have a theoretical xylene loading limit of 8 molc./u.c. around room temperature and $p/p^o = 0.5$. The loading of o-xylene in the conventional crystals were consistent with literature reports, which were slightly smaller than the theoretical value due to some inaccessible sites for the bulkier o-xylene molecule [10,30,31]. The loadings of both xylenes in the ZN-assemblies were larger than those in the conventional crystals. The p-xylene loading in the ZN assembly exceeded the limit of 8 molc./u.c. because of the full accessibility of internal sites and additional inter-sheet sites for adsorption [10]. The improved micropore accessibility also enhanced the o-xylene loading in the ZN plates as compared to the conventional crystals.

Because of the complex structures and broad size distributions of the crystals, we estimated D_T between ranges of average size limits for the ZN plates in assemblies and the conventional crystals based on SEM observations (see ESI). The p-xylene diffusivity in the conventional crystals was in good agreements with literature values measured by the uptake or breakthrough methods [29,32,33]. The ZN assemblies exhibited D_T that was similar to that of the conventional crystals because both allowed p-xylene to enter and diffuse from the straight channels along *b*-axis as well the zigzag channels from the *a-c* direction (Fig. 5F and G).

However, the D_T of o-xylene in the ZN-assembly was dramatically greater by about two orders of magnitude than that in the conventional crystals. Because of its larger kinetic size, o-xylene molecules could only enter the straight channels in b-axis and defuse extremely slowly through the large thickness of the conventional crystals (Fig. 5H). In the conventional crystals, the D_T of o-xylene was roughly 2–3 orders of magnitude smaller than p-xylene also because of the much higher energy barrier for the larger o-xylene molecules to enter and diffuse in the zeolitic channels [27,30,34]. In the multilayered ZN plates, although the zigzag channels are inaccessible to o-xylene, the 1–2 nm-width inter-sheet spaces allow fast transport in the layered structure and then enter the straight channels throughout the thickness (Fig. 5G). In addition, since the constituting single layers were only two cells (total 4 nm length) in thickness, the o-xylene molecules exited from the inner side of the sheets could efficiently move around the inter-sheet spaces to enter the next layers without being blocked by the superimposed layers.

The unique interconnected mesopore and micropore system and the consequent efficient molecular transport mechanisms of the ZN plates were further corroborated by the dynamic adsorption behaviors of p-/o-xylene equimolar vapor mixture. In the conventional crystals, the pseudo D_T derived from the mixture uptake curve was 10 times greater than that of the o-xylene but more than 20 times smaller than that of the p-xylene. Obviously, for the mixture, the intracrystalline diffusion of p-xylene is hindered by the slow-moving o-xylene in the long channels of the large crystals. In contrary, for the ZN plates, the uptake rate and pseudo D_T for the p-/o-xylene mixture were comparable to those of the p-xylene. This confirms that the diffusion of p-xylene in the multilayered ZN plates was much less affected by the coexisting o-xylene because of the effective transport and distribution of xylene molecules through the inter-sheet spaces that is blocked by the o-xylene molecules.

4. Conclusion

A facile self-seeded secondary growth method has been demonstrated for efficient reproduction of flower-like MFI ZN assemblies in single step. These flower-like open architectures consist of very large ZN petals that are mechanically strong to prevent ZN collapse and agglomeration during the thermal activation. Thus, the activated ZN assemblies preserve the unique pore system of interconnected intersheet and intracrystalline micropores for high-efficiency molecular adsorption and diffusion. The activated ZN assemblies allow conveniently harvesting large-sized ZN plates with typical lateral dimensions of 1.5 μm × 2.5 μm. These ZN plates are ~60-nm thick stacks of 4-nm-thick single crystalline nanosheets. The multilayered ZN plate assemblies, because of the unique pore system, exhibited markedly enhanced equilibrium loading and uptake rates in xylene adsorptions when compared to the conventional crystals. The dynamic adsorption behaviors of xylenes have revealed that the multilamellar ZNs offer significantly improved micropore accessibility and apparent diffusivity for critically sized molecules. Thus, the ZN single sheets, the multilayered ZN plates, and the ZN-assemblies have great potential for developing high-performance adsorbents, catalysts, and molecular-sieve membranes.

CRediT authorship contribution statement

Zishu Cao: Writing – original draft, Validation, Methodology, Investigation, Formal analysis, Data curation. **Landysh Iskhakova:** Validation, Investigation, Formal analysis, Data curation. **Xinhui Sun:** Validation, Investigation, Formal analysis, Data curation. **Ninad D. Anjikar:** Validation, Investigation. **Shaowei Yang:** Supervision, Investigation. **Junhang Dong:** Writing – review & editing, Writing – original draft, Supervision, Resources, Project administration, Funding acquisition, Formal analysis, Conceptualization.

Declaration of competing interest

The authors declare that they have no known competing financial interests or personal relationships that could have appeared to influence the work report in this paper.

Acknowledgements

Appendix A. Supplementary data

Supplementary data to this article can be found online at https://doi.org/10.1016/j.micromeso.2022.111854.

References

[1] M. Choi, K. Na, J. Kim, Y. Sakamoto, O. Terasaki, R. Ryoo, Stable single-unit-cell nanosheets of zeolite MFI as active and long-lived catalysts, Nature 461 (2009) 246–249.

[2] K. Na, Park, W.Y. Seo, R. Ryoo, Disordered assembly of MFI zeolite nanosheets with a large volume of intersheet mesopores, Chem. Mater. 23 (2011) 1273–1279.

[3] W.J. Roth, P. Nachtigall, R.E. Morris, J. Čejka, Two-dimensional zeolites: current status and perspectives, Chem. Rev. 114 (2014) 4807–4837.

[4] M.Y. Jeon, D. Kim, P. Kumar, P.S. Lee, N. Rangnekar, P. Bai, M. Shete, B. Elyassi, H. S. Lee, K. Narasimharao, S.N. Basahel, S. Al-Thabaiti, W. Xu, H.J. Cho, E.O. Fetisov, R. Thyagarajan, R.F. DeJaco, W. Fan, K.A. Mkhoyan, J.I. Siepmann, M. Tsapatsis, Ultra-selective high-flux membranes from directly synthesized zeolite nanosheets, Nature 543 (2017) 690–694.

[5] A. Corma, V. Fornes, S.B. Pergher, Th.L.M. Maesen, J.G. Buglass, Delaminated zeolite precursors as selective acidic catalysts, Nature 396 (1998) 353–356.

[6] D. Kerstens, B. Smeyers, J. Van Waeyenberg, Q. Zhang, J. Yu, B.F. Sels, State of the art and perspectives of hierarchical zeolites: practical overview of synthesis methods and use in catalysis, Adv. Mater. 32 (2020), 2004690.

[7] Y. Guefrachi, G. Sharma, D. Xu, G. Kumar, K.P. Vinter, O.A. Abdelrahman, X. Li, S. Alhassan, P.J. Dauenhauer, A. Navrotsky, W. Zhang, M. Tsapatsis, Steam-induced coarsening of single-unit-cell MFI zeolite nanosheets and its effect on external surface Brønsted acid catalysis, Angew. Chem. Int. Ed. 59 (2020) 9579–9585.

[8] L. Meng, X. Zhu, J.M. Hensen, Stable Fe/ZSM-5 nanosheet zeolite catalysts for the oxidation of benzene to phenol, ACS Catal. 7 (2017) 2709–2719.

[9] X. Feng, P. Zhang, Y. Fang, W. Charusiri, J. Yao, X. Gao, Q. Wei, P. Reubroycharoen, T. Vitidsant, Y. Yoneyama, G. Yang, N. Tsubaki, Designing a hierarchical nanosheet ZSM-35 zeolite to realize more efficient ethanol synthesis from dimethyl ether and syngas, Catal. Today 343 (2020) 206–214.

[10] N.S. Kim, N. Numan, S.C. Nam, S.E. Park, C. Jo, Dynamic adsorption/desorption of p-xylene on nanomorphic MFI zeolites: effect of zeolite crystal thickness and mesopore architecture, J. Hazard Mater. 403 (2021) 123659.

[11] G. Sastre, Look beneath the surface, Nat. Mater. 19 (2020) 1040–1046.

[12] D. Kim, Y. Jeon, B.L. Stottrup, M. Tsapatsis, Para-xylene ultra-selective zeolite MFI membranes fabricated from nanosheet monolayers at the air–water interface, Angew. Chem. Int. Ed. 57 (2018) 480–485.

[13] B. Min, S. Yang, A. Korde, Y.H. Kwon, C.W. Jones, S. Nair, Continuous zeolite MFI membranes fabricated from 2D MFI nanosheets on ceramic hollow fibers, Angew. Chem. Int. Ed. 58 (2019) 8201–8205.

[14] H. Zhang, Q. Xiao, X. Guo, N. Li, P. Kumar, N. Rangnekar, S. Al-Thabaiti, M. Y. Jeon, K. Narasimharao, S.N. Basahel, B. Topuz, F.J. Onorato, C.W. Macosko, K. A. Mkhoyan, M. Tsapatsis, Open-pore two-dimensional MFI zeolite nanosheets for the fabrication of hydrocarbon-isomer-selective membranes on porous polymer supports, Angew. Chem. Int. Ed. 55 (2016) 7184–7187.

[15] Z. Cao, S. Zeng, Z. Xu, A. Arvanitis, S. Yang, X. Gu, J. Dong, Ultrathin ZSM-5 zeolite nanosheet laminated membrane for high-flux desalination of concentrated brines, Sci. Adv. 4 (2018), eaau8634.

[16] Z. Cao, L. Iskhakova, X. Sun, Z. Tang, J. Dong, ZSM-5 zeolite nanosheet-based membranes on porous polyvinylidene fluoride for high-flux desalination, ACS Appl. Nano Mater. 4 (3) (2021) 2895–2902.

[17] K. Varoon, X. Zhang, B. Elyassi, D.D. Brewer, M. Gettel, S. Kumar, J.A. Lee, S. Maheshwari, A. Mittal, C.Y. Sung, M. Cococcioni, L.F. Francis, A.V. McCormick, K.A. Mkhoyan, M. Tsapatsis, Dispersible exfoliated zeolite nanosheets and their application as a selective membrane, Science 334 (2011) 72–75.

[18] L. Meng, B. Mezari, M.G. Goesten, E.J.M. Hensen, One-step synthesis of hierarchical ZSM-5 using cetyltrimethylammonium as mesoporogen and structure-directing agent, Chem. Mater. 29 (2017) 4091–4096.

[19] N. Linares, E.O. Jardim, A. Sachse, E. Serrano, J. García-Martínez, The energetics of surfactant-templating of zeolites, Angew. Chem. Int. Ed. 57 (2018) 8724–8728.

[20] C. Peng, Z. Liu, Y. Yonezawa, N. Linares, Y. Yanaba, C.A. Trujillo, T. Okubo, T. Matsumoto, J. García-Martínez, T. Wakih, Testing the limits of zeolite structural flexibility: ultrafast introduction of mesoporosity in zeolites, J. Mater. Chem. 8 (2020) 735–742.

[21] W. Chaikittisilp, Y. Suzuki, R.R. Mukti, T. Suzuki, K. Sugita, K. Itabashi, A. Shimojima, T. Okubo, Formation of hierarchically organized zeolites by sequential intergrowth, Angew. Chem. Int. Ed. 52 (2013) 3355–3359.

[22] G. Bonilla, I. Daz, M. Tsapatsis, H.-K. Jeong, Y. Lee, D.G. Vlachos, Zeolite (MFI) crystal morphology control using organic structure-directing agents, Chem. Mater. 16 (2004) 5697–5705.

[23] Atlas of zeolite framework types, in: C. Baerlocher, L.B. McCusker, D.H. Olson (Eds.), Structure Commission of the International Zeolite Association, seventh ed., Elsevier, Oxford, UK, 2007.

[24] X. Tang, J. Provenzano, Z. Xu, J. Dong, H. Guan, H. Xiao, Acidic ZSM-5 zeolite-coated long period fiber grating for optical sensing of ammonia, J. Mater. Chem. 21 (2011) 181–186.

[25] X. Yang, L. Huang, J. Li, X. Tang, X. Luo, Fabrication of SiO_2@silicalite-1 and its use as a catalyst support, RSC Adv. 7 (2017) 12224–12230.

[26] X. Gu, J. Dong, T.M. Nenoff, D.E. Ozokwelu, Separation of *p*-xylene from multicomponent vapor mixtures using tubular MFI zeolite membranes, J. Membr. Sci. 280 (2006) 624–633.

[27] Z. Lai, G. Bonilla, I. Diaz, J.G. Nery, K. Sujaoti, M. Amat, E. Kokkoli, O. Terasaki, R. W. Thompson, M. Tsapatsis, D.G. Vlachos, Microstructural optimization of a zeolite membrane for organic vapor separation, Science 300 (2003) 456–460.

[28] J. Crank, The Mathematics of Diffusion, Oxford Press, London, 1975.

[29] X. Meng, L. Duan, Q. Wang, J.S. Chung, L. Song, Z. Sun, Thermodynamics and kinetics study of the adsorption and diffusion of p-xylene in silicalite-1, J. Non-Equilib. Thermodyn. 34 (2009) 35–45.

[30] H. Karsh, A. Çulfaz, H. Yiicel, Sorption properties of silicalite-1 of pure silica form: the influence of sorption history on sorption kinetics of critically sized molecules, Zeolites 12 (1992) 728–732.

[31] S. Chempath, R.Q. Snurr, J.J. Low, Molecular modeling of binary liquid-phase Adsorption of aromatics in silicalite, AIChE J. 50 (2004) 463–469.

[32] P. Wu, A. Debebe, Y.H. Ma, Adsorption and diffusion of C6 and C8 hydrocarbons in silicalite, Zeolites 3 (1983) 118–122.

[33] D.B. Shah, H.Y. Liou, Time-lag measurements for diffusion of aromatics through a silicalite membrane, Zeolites 14 (1994) 541–548.

[34] S. Caro-Ortiz, E. Zuidema, M. Rigutto, D. Dubbeldam, T.J.H. Vlugt, Effects of framework flexibility on the adsorption and diffusion of aromatics in MFI-type zeolites, J. Phys. Chem. C 124 (2020) 24488–24499.